Nonlinear Dyn (2018) 92:1935–1945
https://doi.org/10.1007/s11071-018-4172-7

ORIGINAL PAPER

Resonant nonlinearities of piezoelectric macro-fiber composite cantilevers with interdigitated electrodes in energy harvesting

D. Tan · P. Yavarow · A. Erturk

Received: 25 July 2017 / Accepted: 23 February 2018 / Published online: 10 March 2018

Abstract We explore the modeling and analysis of nonlinear nonconservative dynamics of macro-fiber composite (MFC) piezoelectric structures, guided by rigorous experiments, for resonant vibration-based energy harvesting, as well as other applications leveraging the direct piezoelectric effect, such as resonant sensing. The MFCs employ piezoelectric fibers of rectangular cross section embedded in Kapton with interdigitated electrodes to exploit the 33-mode of piezoelectricity. Existing modeling and analysis efforts for resonant nonlinearities have so far considered conventional piezoceramics that use the 31-mode of piezoelectricity. In the present work, we develop a framework to represent and predict nonlinear electroelastic dynamics of MFC bimorph cantilevers under resonant base excitation for primary resonance behavior. The interdigitated electrodes are shunted to a set of resistive electrical loads to quantify the electrical power output. Experiments are conducted on a set of MFC bimorphs over a broad range of mechanical excitation levels to identify the types of nonlinearities present and to compare the harmonic balance model predictions and experiments. The experimentally observed interaction of quadratic piezoelectric material softening and cubic geometric hardening effects is captured and demonstrated by the model. It is shown that the linearized version of the model yields highly inaccurate results for typical base acceleration levels and frequencies involved in vibration energy harvesting, while the nonlinear framework presented here can accurately predict the amplitude-dependent resonant frequency response.

Keywords Nonlinear · Vibration · Piezoelectricity · Energy harvesting · Composites

D. Tan · P. Yavarow · A. Erturk (✉)
G.W. Woodruff School of Mechanical Engineering,
Georgia Institute of Technology, Atlanta, GA, USA
e-mail: alper.erturk@me.gatech.edu

1 Introduction

Piezoelectricity is a reversible process in the form of the direct effect (conversion of mechanical strain to electric charge) and the converse effect (conversion of electric potential to mechanical strain) and has been used in numerous applications ranging from sensing and actuation to vibration control and energy harvesting over the past several decades. The most typical use of piezoelectric materials in bending (flexural) mode is through the utilization of the 31-mode with uniform electrodes. The use of 31-mode in bending has been well studied for sensing, energy harvesting, and static or dynamic actuation for decades [1–13], while the 33-mode has been conventionally used for longitudinal (axial) deformations through the use of piezoelectric stacks and bars [14–19].

It is well known that the 33-mode piezoelectric strain constant is around 50–100% larger than that of the 31-mode. The 33-mode was first utilized in

bending using Active-Fiber Composite (AFC) structures via the implementation of interdigitated electrodes (IDEs) as explored in the early work of Bent and Hagood [20] and Bent et al. [21,22]. The AFC technology used piezoelectric fibers with a circular cross section which limited the contact area between the fibers and electrodes, yielding reduced electromechanical coupling and high dielectric loss. The Macro-Fiber Composite (MFC) technology [23,24] developed at the NASA Langley Research Center overcame this issue by using fibers with rectangular cross section. The MFC piezoelectric materials have been used in structural sensing and vibration control [25,26], bio-inspired locomotion [27,28], acoustic wave devices [29,30], morphing- and flapping-wing structures [31–34], and in-air/underwater dynamic actuation or energy harvesting [27,35–41].

Constitutive modeling and experimental characterization of piezoelectric MFCs have been researched by several groups. Williams et al. [42–44] presented an experimentally validated model for equivalent thermal expansion and mechanical properties of MFCs using modified classical mixing rules. Deraemaeker et al. [45] reported rule of mixtures calculations of the equivalent linear parameters and compared their calculations with manufacturers data and experimental results. Shahab and Erturk [46] coupled homogenized linear constitutive modeling with a geometrically linear Euler–Bernoulli electro-elastodynamics framework for energy harvesting, sensing, and actuation problems. They implemented this linear model for linear underwater bio-inspired actuation and thrust generation [47]. Nonlinear modeling of piezoelectric materials to date has been mostly focused on monolithic piezoelectric materials such as the geometrically linear (for stiff and brittle piezoceramics) and materially nonlinear framework by Leadenham and Erturk [10] (see others in their references).

In the present paper, we aim to develop a geometrically and materially nonlinear framework for resonant mechanical excitation of MFC bimorph cantilevers with a focus on energy harvesting from base excitation. The linear constitutive equations are modified to account for piezoelectric softening while capturing the geometric hardening nonlinearity as well as dissipative effects. In the following, the governing nonlinear electroelastic equations are derived and then solved using the method of harmonic balance. Experimental results are compared with model simulations for a range of base excitation levels and electrical load resistance values, and conclusions are drawn.

2 Nonlinear nonconservative electroelastic equations for an MFC bimorph cantilever under base excitation

For a piezoelectric material utilizing the 33-mode, the electric enthalpy density, H, can be given by

$$H = \frac{1}{2}c_{33}^{E}S_3^2 - \frac{1}{3}\gamma\,|S_3|\,S_3^2 - e_{33}S_3E_3 - \frac{1}{2}\varepsilon_{33}^{S}E_3^2 \quad (1)$$

where c_{33}^{E} is the elastic modulus at constant electric field, S_3 is the strain, E_3 is the electric field, e_{33} is the piezoelectric stress constant, ε_{33}^{S} is the permittivity at constant strain, and γ is a nonlinear strain coefficient to account for ferroelastic softening in PZT-5A [10,48]. (These parameters are defined for the thin structure and therefore reduced from the 3D constitutive equations.) Note that the electromechanical coupling and electric field nonlinearities are neglected since the focus of this work is placed on energy harvesting from mechanical base excitation, yielding relatively low electric fields.

The bending strain at any point in an Euler-Bernoulli cantilever is given by $S_3 = -z\theta_{,s}$, where θ is the angular displacement, z is the distance from the neutral axis, and the subscript s refers to a spatial derivative with respect to the arc length s. Although the electric field is non-uniform within the piezoelectric material, the electric field across two IDEs can be approximated by $E_3 \approx -\dfrac{v}{L_e} = -\dfrac{\dot{\lambda}}{L_e}$, where v is the voltage across the IDEs, $\dot{\lambda}$ is the time derivative of the flux linkage, and L_e is the distance between two IDEs. Therefore, the potential energy corresponding to the piezoelectric material is

$$U_p = \int_0^L \left[\int_0^b \int_0^h \left(\frac{1}{2}c_{33}^{E}z^2\theta_{,s}^2 - \frac{1}{3}\gamma\,|z|\,z^2\,|\theta_{,s}|\,\theta_{,s}^2 - e_{33}z\theta_{,s}\frac{\dot{\lambda}}{L_e} - \frac{1}{2}\frac{\varepsilon_{33}^{S}}{L_e^2}\dot{\lambda}^2 \right) \mathrm{d}z\mathrm{d}y \right] \mathrm{d}x \quad (2)$$

However, as described in Deraemaeker et al. [45] and Shahab and Erturk [46] and illustrated in Fig. 1, the rectangular piezoelectric fibers within an MFC (polarized in the x-direction in Fig. 1) are separated by passive layers of epoxy and then embedded within Kapton film containing interdigitated copper electrodes perpendicular to the piezoelectric fibers, creating an array of

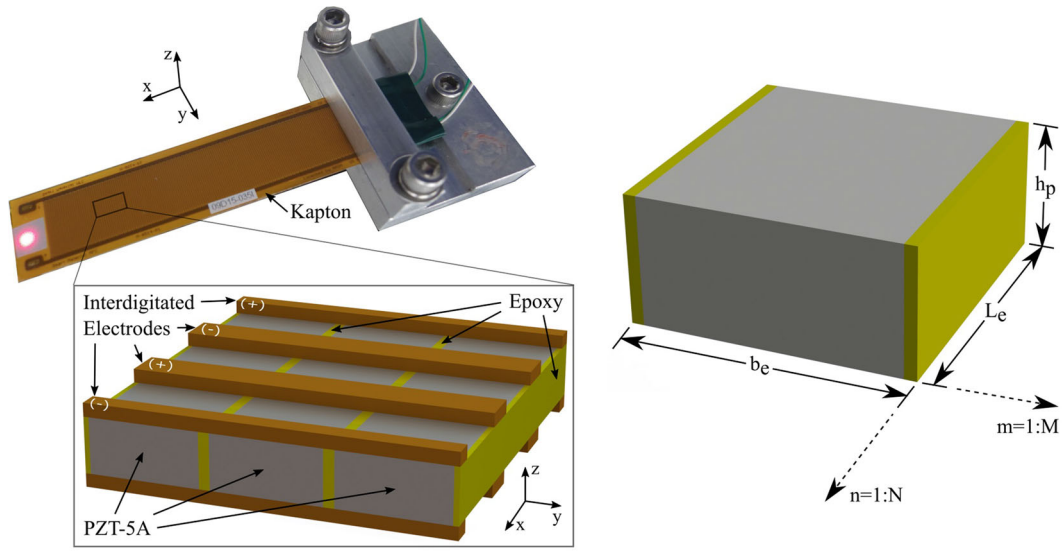

Fig. 1 MFC bimorph cantilever and a close-up of one of its layers showing active piezoelectric fibers separated by epoxy and embedded in Kapton film containing interdigitated copper electrodes (left) and a representative volume element ($M \times N$ representative volume elements exist in an MFC layer) and its effective dimensions (right)

repeating representative volume elements (RVEs) [46]. Each RVE is of width b_e, length L_e, and thickness h_p (as depicted on the right side of Fig. 1) and has material properties defined by the mixing rules (i.e., rule of mixtures) formulation [45,46,49]:

$$
\begin{aligned}
c^E_{33,e} &= \nu c^E_{33,p} + (1-\nu)\, c^E_{33,m} \\
d_{33,e} &= \frac{1}{c^E_{33,e}} \nu d_{33,p} c^E_{33,p} \\
\varepsilon^S_{33,e} &= \left[\nu \varepsilon^T_{33,p} + (1-\nu)\, \varepsilon^T_{33,m}\right] - d^2_{33,e} c^E_{33,e}
\end{aligned}
\tag{3}
$$

where ν is the volume fraction of PZT within a RVE, ε^T_{33} is the permittivity under constant stress, d_{33} is the piezoelectric charge constant, and the subscripts p, m, and e correspond to the piezoelectric fiber properties, the matrix (epoxy) properties, and the equivalent properties of the RVE, respectively. The section of the MFC covered in piezoelectric fibers contains M RVEs in the width direction and N_a RVEs in the length direction, making the active width $b_{\text{act}} = Mb_e$ and the active length $L_{\text{act}} = N_a L_e$. Part of the MFC is clamped in a way that sections of the piezoelectric fibers remain motionless and thus are not strained, so we define the clamped active length as $L = NL_e$.

The MFC bimorph is constructed by bonding two MFCs back to back and wiring them in parallel, so the total potential energy in an MFC bimorph can be written as:

$$
\begin{aligned}
U_p = \int_0^L \Bigg(&\frac{1}{2} E I_p \theta^2_{,s} - \frac{1}{3} \gamma B \left|\theta_{,s}\right| \theta^2_{,s} \\
&- \vartheta_p \dot{\lambda} \left[H(s) - H(s-L)\right] \theta_{,s} - \frac{1}{2} \frac{C_p}{NL_e} \dot{\lambda}^2 \Bigg) \mathrm{d}s
\end{aligned}
\tag{4}
$$

where $H(s)$ is the Heaviside step function, and the distributed material properties of the piezoelectric fibers within the MFC bimorph are

$$
\begin{aligned}
EI_p &= 2 \sum_{m=1}^{M} b_e c_{33,e} \left[\frac{(h_p + h_k)^3 - (h_k)^3}{3} \right] \\
B &= \sum_{m=1}^{M} b_e \left[\frac{(h_p + h_k)^4 - (h_k)^4}{2} \right] \\
\vartheta_p &= 2 \sum_{m=1}^{M} \frac{b_e e_{33,e}}{L_e} \left[\frac{(h_p + h_k)^2 - (h_k)^2}{2} \right] \\
&= 2 \sum_{m=1}^{M} e_{33,e} \frac{b_e h_p}{L_e} \left(\frac{h_p}{2} + h_k \right) \\
&\approx 2 \sum_{m=1}^{M} e_{33,e} \frac{A_e h_{\text{pc}}}{L_e} \\
C_p &= 2 \sum_{m=1}^{M} \sum_{n=1}^{N_a} \varepsilon^S_{33,e} \frac{b_e h_p}{L_e} \approx 2 \sum_{m=1}^{M} \sum_{n=1}^{N_a} \varepsilon^S_{33,e} \frac{A_e}{L_e}
\end{aligned}
\tag{5}
$$

where h_p and h_k correspond to the thickness of the piezoelectric layer and the Kapton layer, respectively, and the effective area A_e is introduced to account for the approximation in the electric field (i.e., A_e is an equivalent RVE area that corresponds to uniform electric field, identified from measured capacitance).

Equation (4) accounts for the potential energy associated with all of the RVEs within the MFC bimorph, but because copper has a higher Young's Modulus than the PZT-5A utilized in the MFC, the strain energy in the Kapton–copper layers is not negligible:

$$\begin{aligned} U_{kc} &= \int_0^L \frac{1}{2} EI_{\mathrm{kc}} \theta_{,s}^2 \mathrm{d}s \\ EI_{\mathrm{kc}} &= 2 \sum_{m=1}^{M} b_e \left(E_c \nu_c + E_k (1-\nu_c)\right) \\ &\quad \left[\frac{h_k^3}{3} + \frac{\left(2h_k + h_p\right)^3 - \left(h_k + h_p\right)^3}{3}\right] \end{aligned} \tag{6}$$

where ν_c is the volume fraction of copper within the Kapton–copper layer (approximately 24%), and the subscripts c, k, and kc refer to the copper properties, the Kapton properties, and the combined Kapton–copper properties, respectively.

The total potential energy for the entire MFC bimorph can therefore be written as

$$\begin{aligned} U = \int_0^L &\left(\frac{1}{2} EI_{\mathrm{eff}} \theta_{,s}^2 - \frac{1}{3}\gamma B \left|\theta_{,s}\right| \theta_{,s}^2 \right. \\ &\left. - \vartheta_p \dot{\lambda} \left[H(s) - H(s-L)\right] \theta_{,s} - \frac{1}{2} \frac{C_p}{NL_e} \dot{\lambda}^2 \right) \mathrm{d}s \end{aligned} \tag{7}$$

where $EI_{\mathrm{eff}} = EI_p + EI_{\mathrm{kc}}$, and the kinetic energy can be written as

$$T = \frac{1}{2} m_s \int_0^L \left[{u_{x,t}}^2 + \left(u_{z,t} + u_{b,t}\right)^2\right] \mathrm{d}s \tag{8}$$

where m_s is the structural mass per length of the MFC bimorph and u_b is the base displacement.

For an inextensible cantilever, the Lagrangian $\mathcal{L} = T - U$ needs to include a Lagrange multiplier, Λ, to account for the inextensibility condition [50–52]:

$$\begin{aligned} \mathcal{L} = &\frac{1}{2} m_s \int_0^L \left[{u_{x,t}}^2 + \left(u_{z,t} + u_{b,t}\right)^2\right] \mathrm{d}s \\ &- \frac{1}{2} \Lambda \int_0^L \left[\left(1 + u_{x,s}\right)^2 + \left(u_{z,s}\right)^2 - 1\right] \mathrm{d}s + \\ &- \int_0^L \left(\frac{1}{2} EI_{\mathrm{eff}} \theta_{,s}^2 - \frac{1}{3}\gamma B \left|\theta_{,s}\right| \theta_{,s}^2 \right. \\ &\left. - \vartheta_p \dot{\lambda} \left[H(s) - H(s-L)\right] \theta_{,s} - \frac{1}{2} \frac{C_p}{NL_e} \dot{\lambda}^2 \right) \mathrm{d}s \end{aligned} \tag{9}$$

Applying Hamilton's principle, $\int_{t_1}^{t_2} \left(\delta \mathcal{L} + \delta W_{\mathrm{NC}}\right) \mathrm{d}t = 0$, where the virtual nonconservative work on the structure includes linear structural damping and electrical dissipation over a resistive load (of resistance R), $\delta W_{\mathrm{NC}} = \int_0^L \left(-c_z u_{z,t} \delta u_z - \frac{\dot{\lambda}}{R} \delta\lambda\right) \mathrm{d}s$, we find

$$\int_{t_1}^{t_2} \left\{ \begin{array}{l} \int_0^L \left(\begin{array}{l} m_s u_{x,t} \delta u_{x,t} + m_s \left(u_{z,t} + u_{b,t}\right) \delta u_{z,t} - c_z u_{z,t} \delta u_z \\ -\Lambda (1 + u_{x,s}) \delta u_{x,s} - \Lambda u_{z,s} \delta u_{z,s} \\ + \left(\begin{array}{l} -EI_{\mathrm{eff}} \theta_{,s} + \gamma B \theta_{,s}^2 \mathrm{sgn}(\theta_{,s}) \\ +\vartheta_p \dot{\lambda} \left[H(s) - H(s-L)\right] \end{array} \right) \delta\theta_{,s} \end{array} \right) \mathrm{d}s \\ + \left(\int_0^L \vartheta_p \theta_{,s} \left[H(s) - H(s-L)\right] \mathrm{d}s + C_p \dot{\lambda} \right) \delta\dot{\lambda} \\ - \int_0^L \frac{\dot{\lambda}}{R} \delta\lambda \mathrm{d}s \end{array} \right\} \mathrm{d}t = 0 \tag{10}$$

First converting from angular displacements into x- and z-displacements, and then integrating by parts, Hamilton's principle yields three equations of motion (nonlinearities kept to cubic order):

$$\begin{aligned} &\left[\Lambda (1 + u_{x,s}) + EI_{\mathrm{eff}} \left(u_{z,s} u_{z,sss}\right) \right. \\ &\left. - \left(\vartheta_p \dot{\lambda} \left[H(s) - H(s-L)\right]\right)_{,s} u_{z,s} \right]_{,s} = m_s u_{x,tt} \\ &\left[\begin{array}{l} \Lambda u_{z,s} - EI_{eff} \left(u_{z,sss} + u_{z,s} u_{z,ss}^2\right) + 2\gamma B \left|u_{z,ss}\right| u_{z,sss} \\ + \left(\vartheta_p \dot{\lambda} \left[H(s) - H(s-L)\right]\right)_{,s} \left(1 + u_{x,s}\right) \end{array} \right]_{,s} \end{aligned}$$

$$c_z u_{z,t} - m_s u_{b,tt} = m_s u_{z,tt} - \int_0^L \vartheta_p \left((1+u_{x,s})u_{z,ss} - u_{z,s}u_{x,ss}\right)_{,t} \mathrm{d}s - C_p \ddot{\lambda} - \frac{\dot{\lambda}}{R} = 0 \tag{11}$$

By spatial integration for u_x and utilizing the appropriate boundary conditions, the Lagrange multiplier becomes

$$\Lambda = -EI_{\text{eff}} u_{z,s} u_{z,sss} - \frac{1}{2} m_s \int_L^s \left(\int_0^\delta u_{z,\xi}^2 d\xi \right)_{,tt} \mathrm{d}\delta + \left(\vartheta_p \dot{\lambda} \left[H(x) - H(x-L)\right]\right)_{,s} u_{z,s} \tag{12}$$

which can be substituted into the equation for u_z to find

$$\begin{bmatrix} m_s u_{z,tt} + c_z u_{z,t} + \frac{1}{2} m_s \left[u_{z,s} \int_L^s \left(\int_0^\delta u_{z,\xi}^2 d\xi \right)_{,tt} \mathrm{d}\delta \right]_{,s} \\ + EI_{\text{eff}} \left(u_{z,sss} + u_{z,s} \left(u_{z,s} u_{z,ss} \right)_{,s} \right)_{,s} - 2\gamma B \left(\left| u_{z,ss} \right| u_{z,sss} \right)_{,s} \\ - \vartheta_p v \left[\frac{\partial \delta(x)}{\partial s} - \frac{\partial \delta(x-L)}{\partial s} \right] - \vartheta_p v \left[\delta(x) - \delta(x-L) \right] \left(u_{z,s} u_{z,ss} \right) \end{bmatrix} = -m_s u_{b,tt}$$

$$C_p \dot{v} + \frac{v}{R} + \int_0^L \vartheta_p \left(u_{z,ss} + \frac{1}{2} u_{z,s}^2 u_{z,ss} \right)_{,t} \mathrm{d}s = 0 \tag{13}$$

If the base motion is harmonic about the first natural frequency of the structure, then a single mode assumption can be made for primary resonance behavior, $u_z(s,t) = \phi(s)\eta(t)$, where $\phi(s)$ is the mass normalized first mode shape of a cantilever,

$$\phi(s) = A_1 \left(\cos \frac{\lambda_1 s}{L} - \cosh \frac{\lambda_1 s}{L} + \sigma \left(\sin \frac{\lambda_1 s}{L} - \sinh \frac{\lambda_1 s}{L} \right) \right)$$

$$\sigma = \frac{\sin \lambda_1 - \sinh \lambda_1}{\cos \lambda_1 + \cosh \lambda_1}$$

$$\lambda_1 = 1.8751$$

$$\int_0^L m_s \phi_i(s) \phi_j(s) \mathrm{d}s = \delta_{ij} \tag{14}$$

This results in the equations of motion in modal coordinates,

$$m^* \ddot{\eta} + c^* \dot{\eta} + k^* \left(1 - \gamma^* |\eta|\right) \eta + \frac{\alpha^*}{L^2} \eta^3 + \frac{\beta^*}{L^2} \left(\eta \dot{\eta}^2 + \eta^2 \ddot{\eta} \right) - \theta_p v - \theta_{\text{NL}} v \eta^2 = G^* \cos \Omega t$$

$$C_p \dot{v} + \frac{v}{R} + \theta_p \dot{\eta} + \theta_{\text{NL}} \eta^2 \dot{\eta} = 0 \tag{15}$$

which can be converted back into the measurement coordinates by $w = w(L_m, t) = \phi(L_m)\eta(t)$, where L_m is the distance from the base of the cantilever where the velocity is experimentally measured, yielding the final equations of motion which account for nonlinear strain and the inextensibility condition of a cantilever:

$$\hat{m} \ddot{w} + \hat{c} \dot{w} + \hat{k} \left(1 - \hat{\gamma} |w|\right) w + \frac{\hat{\alpha}}{L^2} w^3 + \frac{\hat{\beta}}{L^2} \left(w \dot{w}^2 + w^2 \ddot{w} \right) - \theta_p v - \frac{\theta_{\text{NL}}}{\phi^2(L_m)} v w^2 = \hat{G} \cos \Omega t$$

$$C_p \dot{v} + \frac{v}{R} + \frac{\theta_p}{\phi(L_m)} \dot{w} + \frac{\theta_{\text{NL}}}{\phi^3(L_m)} w^2 \dot{w} = 0 \tag{16}$$

where

$$\hat{m} = \frac{m_s \int_0^L \phi^2(s) \mathrm{d}s}{\phi(L_m) \int_0^L \phi(s) \mathrm{d}s},$$

$$\hat{\gamma} = \frac{2\gamma B \int_0^L \phi(s) \left(\phi''(s) \phi'''(s) \right)' \mathrm{d}s}{EI_{\text{eff}} \phi(L_m) \int_0^L \phi(s) \phi''''(s) \mathrm{d}s},$$

$$\hat{c} = \frac{c_z \int_0^L \phi^2(s) \mathrm{d}s}{\phi(L_m) \int_0^L \phi(s) \mathrm{d}s},$$

$$\hat{\alpha} = \frac{EI_{eff} L^2 \int_0^L \phi(s) \left\{ \phi'(s) \left(\phi'(s) \phi''(s) \right)' \right\}' \mathrm{d}s}{\phi^3(L_m) \int_0^L \phi(s) \mathrm{d}s},$$

$$\hat{k} = \frac{EI_{\text{eff}} \int_0^L \phi(s) \phi''''(s) \mathrm{d}s}{\phi(L_m) \int_0^L \phi(s) \mathrm{d}s},$$

$$\hat{\beta} = \frac{m_s L^2 \int_0^L \phi(s) \left[\phi'(s) \int_L^s \int_0^\delta \phi'(s)^2 d\xi \mathrm{d}\delta \right]' \mathrm{d}s}{\phi^3(L_m) \int_0^L \phi(s) \mathrm{d}s},$$

$$\theta_p = \vartheta_p \phi'(L), \quad \theta_{\text{NL}} = \frac{1}{2} \vartheta_p \left(\phi'(L) \right)^3,$$

$$\hat{G} = m_s a_b \tag{17}$$

where $\hat{m}$, $\hat{c}$, and $\hat{k}$ are the equivalent linear mass, damping, and stiffness terms, $\hat{\gamma}$ accounts for piezoelectric softening, $\hat{\alpha}$ is the geometric hardening coefficient,

$\hat{\beta}$ is the inertial softening coefficient, θ_p is the linear electromechanical coupling coefficient, θ_{NL} is the nonlinear electromechanical coupling coefficient resulting from nonlinear strain, and $\hat{G}$ is the forcing term.

The coupled ODEs given by Eq. (16) are solved using the method of harmonic balance [53] for all resistive loads and acceleration levels considered in the experiments. Since the base excitation is assumed to be harmonic with a driving frequency Ω, the mechanical response solution and voltage output are expected to have the same period as the mechanical excitation and can be approximated by truncated Fourier series expansions,

$$w_Q = \sum_{q=1}^{Q} \left[a_q \cos(q\Omega t) + b_q \sin(q\Omega t) \right]$$
$$v_Q = \sum_{q=1}^{Q} \left[c_q \cos(q\Omega t) + d_q \sin(q\Omega t) \right] \tag{18}$$

where Q is the number of harmonics considered and the typical constant terms a_0 and c_0 in the Fourier series expansions are zero because of the symmetry of the structure. Substituting the approximate solutions into Eq. (16) results in the residual functions

$$R_1 = \begin{cases} \hat{m}\ddot{w}_Q + \hat{c}\dot{w}_Q + \hat{k}\left(1 - \hat{\gamma}\left|w_Q\right|\right) w_Q + \dfrac{\hat{\alpha}}{L^2} w_Q^3 \\ \quad + \dfrac{\hat{\beta}}{L^2}\left(w_Q \dot{w}_Q^2 + w_Q^2 \ddot{w}_Q\right) \\ \quad - \left(\theta_p + \dfrac{\theta_{\mathrm{NL}}}{\phi^2(L_m)} w_Q^2\right) v_Q - \hat{G}\cos\Omega t \end{cases}$$
$$R_2 = C_p \dot{v}_Q + \frac{v_Q}{R} + \frac{\theta_p}{\phi(L_m)}\dot{w}_Q + \frac{\theta_{\mathrm{NL}}}{\phi^3(L_m)} w_Q^2 \dot{w}_Q \tag{19}$$

Then, using the Galerkin method of mean weighted residuals,

$$\begin{matrix} \int_0^{2\pi/\Omega} R_1 \cos(q\Omega t)\mathrm{d}t = 0, & \int_0^{2\pi/\Omega} R_2 \cos(q\Omega t)\mathrm{d}t = 0 \\ \int_0^{2\pi/\Omega} R_1 \sin(q\Omega t)\mathrm{d}t = 0, & \int_0^{2\pi/\Omega} R_2 \sin(q\Omega t)\mathrm{d}t = 0 \end{matrix} \quad q = 1, \ldots, Q \tag{20}$$

a system of $4Q$ algebraic equations for the Fourier coefficients a_q, b_q, c_q, d_q can be generated. Here we choose to include $Q = 5$ harmonics, resulting in 20 equations and 20 unknowns. These equations can be solved using a multivariate Newton–Raphson method. Since resonant excitation of the nonlinear structure results in a saddle node bifurcation, the Fourier coefficients were first solved for an off-resonance excitation frequency, and then the driving frequency Ω was linearly swept up and down around the first natural frequency using the previous solutions for the Fourier coefficients as seed values in the Newton–Raphson method in order to capture both the high- and low-energy stable solutions of the bifurcation. Another method to analyze the overall nonlinear behavior is by using a multiple scales approach [53] on the equation of motion in the short circuit condition. This method yields an equivalent nondimensional cubic nonlinearity coefficient which combines the effect of the geometric hardening from $\hat{\alpha}$ and the inertial softening from $\hat{\beta}$:

$$\alpha_{\mathrm{eq}} = \frac{\hat{\alpha}}{\hat{k}} - \frac{2}{3}\frac{\hat{\beta}}{\hat{m}} \tag{21}$$

which is expected to be positive for the first bending mode, indicating that the geometric hardening term dominates the third-order behavior of the system.

Table 1 Dimensions and material properties of the MFC bimorph

Property	Symbol	Value
Active length	L_{act}	85 mm
Clamped active length	L	75.5 mm
Clamped overall length	L_{o}	83.5 mm
Active width	b_{act}	7 mm
Total thickness	h	0.61 mm
Measured capacitance	C_p	3.40 nF
First natural frequency (SC)	f_{SC}	40.5 Hz

3 Experimental setup

Two MFCs, model M8507-P1 from Smart Material Corp., were vacuum bonded together without a substrate to form a bimorph structure, the dimensions and material properties of which are listed in Table 1. The sample was then placed in an aluminum clamp and onto an APS 113 Electro-Seis long stroke shaker, as shown in Fig. 2. An accelerometer was mounted to the base of the clamp using wax, and the velocity of the MFC bimorph was measured near the free end of the cantilever with a Polytec OFV-505 laser Doppler vibrometer. The MFC samples in the bimorph were wired in

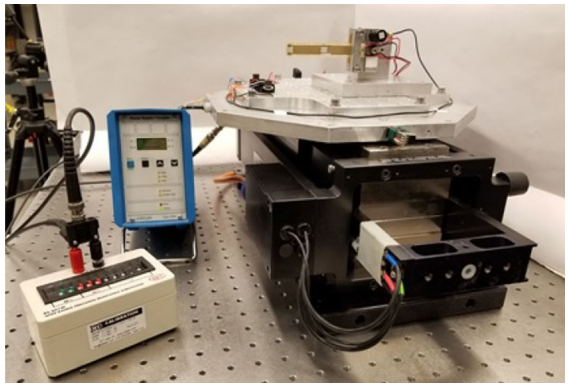

Fig. 2 Cantilevered MFC bimorph mounted on a long stroke shaker for base excitation and shunted to a resistive electrical load box

parallel and placed in the short circuit condition. Linear noise burst experiments were performed to identify the fundamental short circuit (SC) resonance frequency (which is approximately the SC natural frequency due to low damping) and then repeated for resistive loads of 1 kΩ, 1.3 MΩ, and 100 MΩ.

Using a VCS 201 vibration controller, the root-mean-square (RMS) acceleration level was set to $0.5g$ and an up and down frequency sweep was performed around the first short circuit natural frequency at 1 Hz/min. The frequency sweep was repeated at $0.4g$, $0.3g$, $0.2g$, and $0.1g$ RMS, for the cases of resistive loads of a short circuit, 1 kΩ, 1.3 MΩ and 100 MΩ. The base acceleration level, tip velocity of the MFC bimorph, as well as the voltage across the resistive load were measured using an NI-9223 data acquisition device during the nonlinear frequency sweeps.

4 Results

4.1 Experimental results

Figure 3 shows the mechanical and electrical response of the MFC bimorph under base excitation under various resistive loads including only the data corresponding to the downward frequency sweep for clarity. For all acceleration levels and resistive loads considered, the quadratic piezoelectric softening dominates the nonlinear behavior (resulting in an initially linear backbone curve bent to the left), but when the response amplitude is high enough, the third-order geometric hardening behavior becomes visible as expected for the first mode of an inextensible cantilever (resulting in a quadratic bend of the backbone curve back to the right).

Using the RMS velocity data under the short circuit condition, one can plot the detuning of the excitation frequency relative to the short circuit natural frequency versus the response amplitude in meters and then create a backbone curve by applying a polynomial fit over the points corresponding to the maximum response amplitudes, as shown in Fig. 4. This polynomial is of the form $\sigma = C_1 a^2 + C_2 a + C_3$, where σ is the detuning and a is the response amplitude. The nonlinear quadratic piezoelectric softening coefficient $\hat{\gamma}$ and the overall nondimensional cubic nonlinearity coefficient α_{eq} can be approximated from this polynomial by:

$$\hat{\gamma} = \frac{1 - \left(1 - \frac{\sigma_1}{\omega_n}\right)}{a_1}$$
$$\alpha_{\text{eq}} = \frac{8 C_1 L^2}{3\omega_n} \tag{22}$$

where a_1 is a small response amplitude and σ_1 is the detuning corresponding to that small response amplitude, which results in $\hat{\gamma} = 155.32 \frac{1}{m}$ and $\alpha_{\text{eq}} = 98.75$ for this sample.

4.2 Theoretical results

Using the measured capacitance of the MFC bimorph, the effective area A_e was calculated to be 0.0446 mm^2. The coefficients found in Eq. (16) were then calculated using Eqs. (3), (5), and (17), as well as with the parameters extracted from the experimental results using Eq. (22). The nonlinear equations of motion given by Eq. (16) were then solved using the method of harmonic balance for all resistive loads and acceleration levels considered in the experiments as explained previously. The calculated velocity response and output voltage are plotted in Fig. 5.

Both the experimental and theoretical RMS voltage plots for the optimal resistive load (1.3 MΩ) were converted into the average power plot using $P_{\text{avg}} = \frac{V_{\text{RMS}}^2}{R}$ for all base acceleration levels considered, as shown in Fig. 6. The theoretical model shows good agreement with the experiments performed, accurately predicting the maximum power output as well as the jump frequencies. However, the theoretical model slightly overpredicts the output voltage and subsequently underpredicts the mechanical response of the MFC bimorph can-

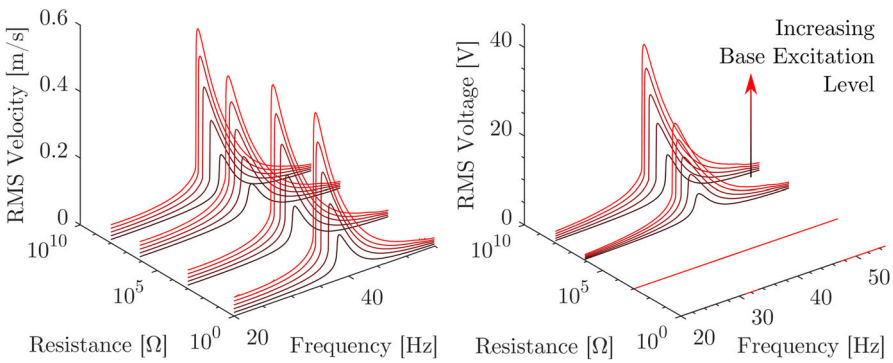

Fig. 3 Measured RMS tip velocity and output voltage of the MFC bimorph versus resistive load and frequency at RMS base acceleration levels of 0.1g, 0.2g, 0.3g, 0.4g, and 0.5g using a downward frequency sweep (increasing base acceleration level from black to red). (Color figure online)

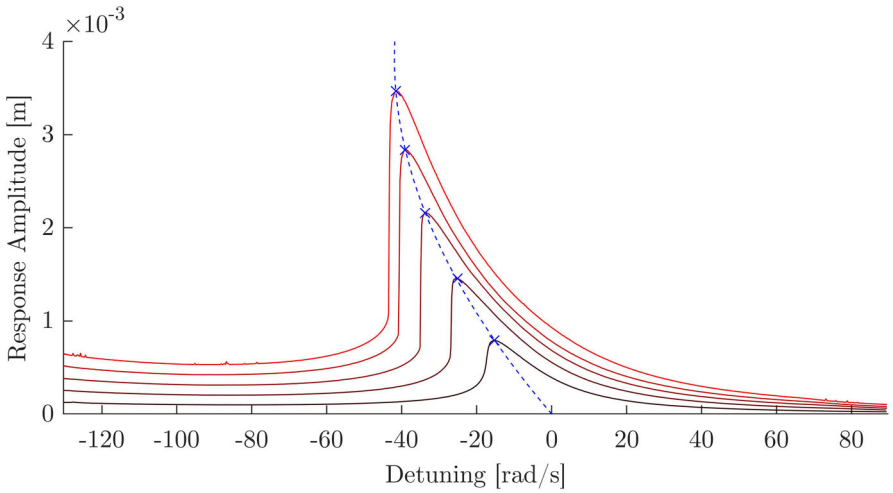

Fig. 4 Experimentally determined response amplitude under the short circuit condition versus detuning relative to the short circuit natural frequency and the corresponding quadratic backbone curve. (Color figure online)

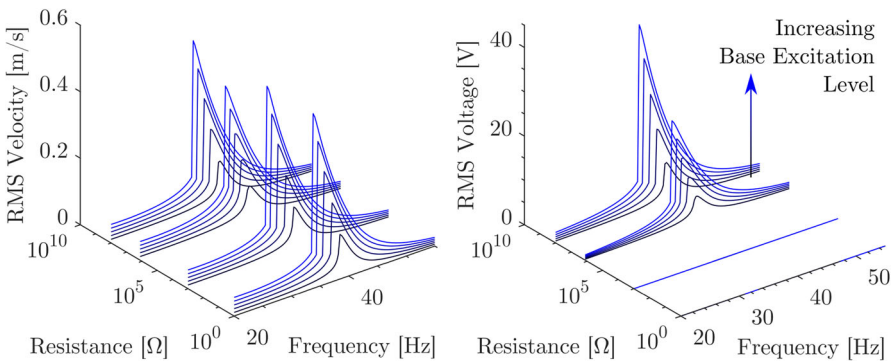

Fig. 5 Theoretical RMS tip velocity and output voltage of the MFC bimorph versus resistive load and frequency at RMS base acceleration levels of 0.1g, 0.2g, 0.3g, 0.4g, and 0.5g using a downward frequency sweep (increasing base acceleration level from black to blue). (Color figure online)

tilever. This discrepancy is likely due to other dissipative terms in the electrical domain (e.g., dielectric loss) not accounted for in the present work.

The nonlinear governing equations given by Eq. (16) were linearized by setting the nonlinear coefficients $\hat{\gamma}$, $\hat{\alpha}$, $\hat{\beta}$, and θ_{NL} to zero. The theoretical average power for the five acceleration levels considered was calculated for various resistive loads at 37, 38, 39, and 40 Hz utilizing both the linearized model and the nonlinear model presented in this work, and the results are compared with the experimental results in Fig. 7. As expected, the linearized model shows the highest output power near the linear resonance frequency of the structure (around 40.5 Hz) and decreased output power as the driving frequency moves away from the linear resonance. The predictions of the linearized model are highly inaccurate for the realistic base acceleration levels considered in this work. The experimental data shown in Fig. 3

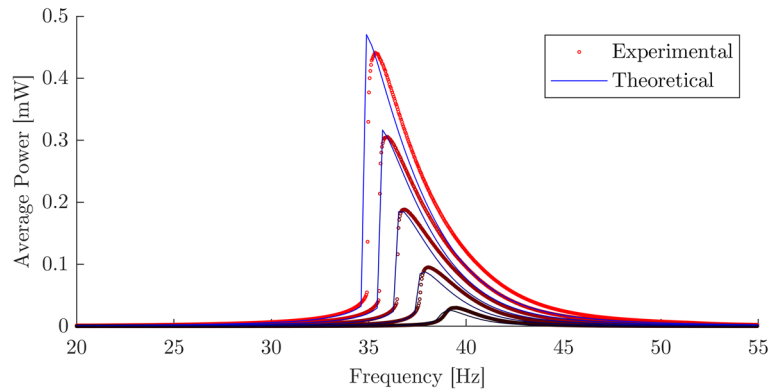

Fig. 6 Experimental (red circles) and theoretical (blue lines) average power at RMS base acceleration levels of 0.1g, 0.2g, 0.3g, 0.4g, and 0.5g using a downward frequency sweep with a resistive load of 1.3 MΩ. (Color figure online)

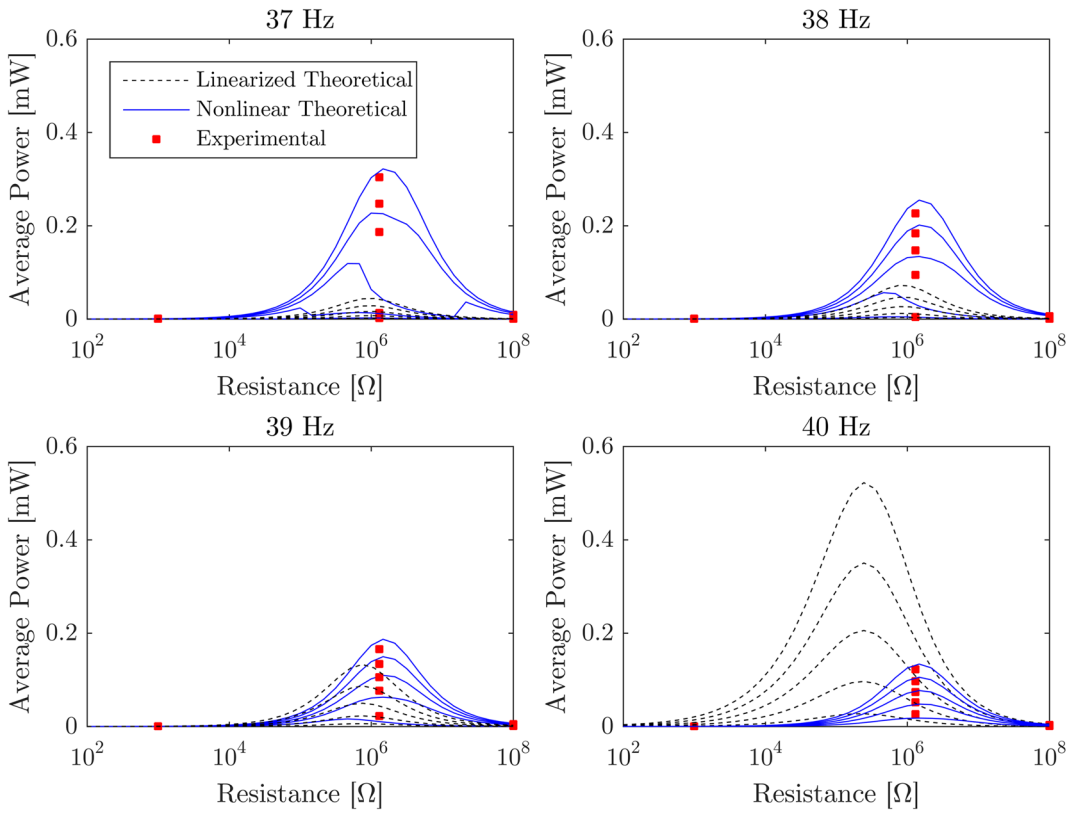

Fig. 7 Theoretical average power utilizing a linearized model (black dashed lines) and the fully nonlinear model (blue solid lines), as well as experimentally determined average power (red markers) at RMS base acceleration levels of 0.1g, 0.2g, 0.3g, 0.4g, and 0.5g using a downward frequency sweep for various resistive loads sampled at 37, 38, 39, and 40 Hz. (Color figure online)

exhibit strong quadratic piezoelectric softening behavior, resulting in larger response amplitudes at frequencies below the short circuit natural frequency which the fully nonlinear model accurately predicts. As the base acceleration level increases, this nonlinear behavior becomes more pronounced, leading to drastically increased errors in the linearized model.

5 Conclusions

A nonlinear nonconservative electroelastic modeling framework was developed for energy harvesting applications from base excitation of the 33-mode of an MFC bimorph cantilever around its first bending mode. The equivalent electromechanical properties of the MFC

bimorph were calculated using a mixing rules formulation, and the effective area of a single RVE as well as piezoelectric softening coefficient were extracted experimentally from the short circuit base excitation case. The equations were solved for primary resonance behavior using the method of harmonic balance for multiple base acceleration levels, and the results were experimentally validated over a range of resistive electrical loads and excitation frequencies. The experimentally observed nonlinear dynamics, which includes quadratic material softening, cubic geometric hardening, cubic inertial softening, and a nonlinear electromechanical coupling term resulting from geometric effects, were all accommodated by the nonlinear model. It was shown that the linearized model yields highly inaccurate results for the realistic base acceleration levels considered in this work for typical ambient vibration frequencies, while the nonlinear model proposed in this work yields very accurate representation and prediction of the governing dynamics. This framework successfully captures the dynamics of MFC structures for energy harvesting and sensing applications with relatively weak electric fields. For applications such as resonant actuation with higher electric fields, additional terms (e.g., coupling nonlinearities, electric field nonlinearities, dielectric losses) may be required and can be incorporated in a similar procedure.

Acknowledgements This work was supported in part by the NSF Grant CMMI-1254262, which is gratefully acknowledged.

References

1. Hagood, N.W., Chung, W.H., von Flotow, A.: Modeling of piezoelectric actuator dynamics for active structural control. J. Intell. Mater. Syst. Struct. **1**, 327–354 (1990)
2. Hagood, N.W., von Flotow, A.: Damping of structural vibrations with piezoelectric materials and passive electrical networks. J. Sound Vib. **146**(2), 243–268 (1991)
3. Smits, J.G., Choi, W.S.: The constituent equations of piezoelectric heterogeneous bimorphs. IEEE Trans. Ultrason. Ferroelectr. Freq. Control **38**(3), 256–270 (1991)
4. Dosch, J.J., Inman, D.J., Garcia, E.: A self-sensing piezoelectric actuator for collocated control. J. Intell. Mater. Syst. Struct. **3**(1), 166–185 (1992)
5. Baz, A., Ro, J.: Vibration control of plates with active constrained layer damping. Smart Mater. Struct. **5**(3), 272 (1996)
6. Leo, D.J.: Engineering Analysis of Smart Material Systems. Wiley, Hoboken (2007)
7. Erturk, A., Inman, D.J.: An experimentally validated bimorph cantilever model for piezoelectric energy harvesting from base excitations. Smart Mater. Struct. **18**(2), 025009 (2009)
8. Erturk, A., Inman, D.J.: Piezoelectric Energy Harvesting. Wiley, Chichester (2011)
9. Erturk, A.: Assumed-modes modeling of piezoelectric energy harvesters: Euler–Bernoulli, Rayleigh, and Timoshenko models with axial deformations. Comput. Struct. **106**, 214–227 (2012)
10. Leadenham, S., Erturk, A.: Unified nonlinear electroelastic dynamics of a bimorph piezoelectric cantilever for energy harvesting, sensing, and actuation. Nonlinear Dyn. **79**(3), 1727–1743 (2015)
11. Leadenham, S., Erturk, A.: Nonlinear M-shaped broadband piezoelectric energy harvester for very low base accelerations: primary and secondary resonances. Smart Mater. Struct. **24**(5), 055021 (2015)
12. Yuan, T., Yang, J., Chen, L.: Experimental identification of hardening and softening nonlinearity in circular laminated plates. Int. J. Non Linear Mech. **95**, 296–306 (2017)
13. Yuan, T., Yang, J., Chen, L.: Nonlinear characteristic of a circular composite plate energy harvester: experiments and simulations. Nonlinear Dyn. **90**(4), 2495–2506 (2017)
14. Feenstra, J., Granstrom, J., Sodano, H.: Energy harvesting through a backpack employing a mechanically amplified piezoelectric stack. Mech. Syst. Signal Process. **22**(3), 721–734 (2008)
15. Cunefare, K.A., Skow, E.A., Erturk, A., Savor, J., Verma, N., Cacan, M.R.: Energy harvesting from hydraulic pressure fluctuations. Smart Mater. Struct. **22**(2), 025036 (2013)
16. Zhao, S., Erturk, A.: Deterministic and band-limited stochastic energy harvesting from uniaxial excitation of a multilayer piezoelectric stack. Sens. Actuators A Phys. **214**, 58–65 (2014)
17. Skow, E.A., Cunefare, K.A., Erturk, A.: Power performance improvements for high pressure ripple energy harvesting. Smart Mater. Struct. **23**(10), 104011 (2014)
18. Shahab, S., Erturk, A.: Contactless ultrasonic energy transfer for wireless systems: acoustic-piezoelectric structure interaction modeling and performance enhancement. Smart Mater. Struct. **23**(12), 125032 (2014)
19. Shahab, S., Gray, M., Erturk, A.: Ultrasonic power transfer from a spherical acoustic wave source to a free-free piezoelectric receiver: modeling and experiment. J. Appl. Phys. **117**(10), 104903 (2015)
20. Bent, A.A., Hagood, N.W.: Piezoelectric fiber composites with interdigitated electrodes. J. Intell. Mater. Syst. Struct. **8**(11), 903–919 (1997)
21. Bent, A.A.: Active fiber composites for structural actuation. Thesis (1997)
22. Bent, A.A., Hagood, N.W., Rodgers, J.P.: Anisotropic actuation with piezoelectric fiber composites. J. Intell. Mater. Syst. Struct. **6**(3), 338–349 (1995)
23. Wilkie, W.K., Bryant, R.G., High, J.W., Fox, R.L., Hellbaum, R.F., Jalink, A., Jr., Little, B.D., Mirick, P.H.: Low-cost piezocomposite actuator for structural control applications. In: SPIE's 7th Annual International Symposium on Smart Structures and Materials, pp. 323–334. International Society for Optics and Photonics
24. Wilkie, W.K., High, J.W.: Method of fabricating NASA-standard macro-fiber composite piezoelectric actuators, NASA/TM-2003-212427, NASA (2003)

25. Browning, J.S.: F-16 ventral fin buffet alleviation using piezoelectric actuators. Thesis (2009)
26. Sodano, H.A., Park, G., Inman, D.J.: An investigation into the performance of macro-fiber composites for sensing and structural vibration applications. Mechan. Syst. Signal Process. **18**(3), 683–697 (2004)
27. Erturk, A., Delporte, G.: Underwater thrust and power generation using flexible piezoelectric composites: an experimental investigation toward self-powered swimmer-sensor platforms. Smart Mater. Struct. **20**(12), 125013 (2011)
28. Cen, L., Erturk, A.: Bio-inspired aquatic robotics by untethered piezohydroelastic actuation. Bioinspir. Biomim. **8**(1), 016006 (2013)
29. Collet, M., Ruzzene, M., Cunefare, K.A.: Generation of lamb waves through surface mounted macro-fiber composite transducers. Smart Mater. Struct. **20**(2), 025020 (2011)
30. Matt, H.M., di Scalea, F.L.: Macro-fiber composite piezoelectric rosettes for acoustic source location in complex structures. Smart Mater. Struct. **16**(4), 1489 (2007)
31. Kim, D.K., Han, J.H.: Smart flapping wing using macrofiber composite actuators. In: Smart Structures and Materials, pp. 61730F. International Society for Optics and Photonics, Bellingham
32. Kim, D.K., Kim, H.I., Han, J.H., Kwon, K.J.: Experimental investigation on the aerodynamic characteristics of a biomimetic flapping wing with macro-fiber composites. J. Intell. Mater. Syst. Struct. **19**(3), 423–431 (2008)
33. Bilgen, O., Kochersberger, K.B., Inman, D.J., Ohanian, O.J.: Novel, bidirectional, variable-camber airfoil via macro-fiber composite actuators. J. Aircr. **47**(1), 303–314 (2010)
34. Paradies, R., Ciresa, P.: Active wing design with integrated flight control using piezoelectric macro fiber composites. Smart Mater. Struct. **18**(3), 035010 (2009)
35. Cha, Y., Kim, H., Porfiri, M.: Energy harvesting from underwater base excitation of a piezoelectric composite beam. Smart Mater. Struct. **22**(11), 115026 (2013)
36. Shahab, S., Erturk, A.: Electrohydroelastic dynamics of macro-fiber composites for underwater energy harvesting from base excitation. In: SPIE Smart Structures and Materials+ Nondestructive Evaluation and Health Monitoring, vol. 9057, pp. 90570C. International Society for Optics and Photonics, Bellingham
37. Shahab, S., Erturk, A.: Underwater dynamic actuation of macro-fiber composite flaps with different aspect ratios: electrohydroelastic modeling, testing, and characterization. In: ASME 2014 Conference on Smart Materials, Adaptive Structures and Intelligent Systems, pp. V002T06A007. American Society of Mechanical Engineers
38. Shahab, S., Erturk, A.: Unified electrohydroelastic investigation of underwater energy harvesting and dynamic actuation by incorporating Morison's equation. In: SPIE Smart Structures and Materials+ Nondestructive Evaluation and Health Monitoring, pp. 94310C. International Society for Optics and Photonics
39. Shahab, S., Erturk, A.: Experimentally validated nonlinear electrohydroelastic Euler-Bernoulli-Morison model for macro-fiber composites with different aspect ratios. In: ASME 2015 International Design Engineering Technical Conferences and Computers and Information in Engineering Conference, pp. V008T13A030. American Society of Mechanical Engineers
40. Shahab, S., Tan, D., Erturk, A.: Hydrodynamic thrust generation and power consumption investigations for piezoelectric fins with different aspect ratios. Eur. Phys. J. Spec. Top. **224**(17–18), 3419–3434 (2015)
41. Cha, Y., Chae, W., Kim, H., Walcott, H., Peterson, S.D., Porfiri, M.: Energy harvesting from a piezoelectric biomimetic fish tail. Renew. Energy **86**, 449–458 (2016)
42. Williams, R.B., Inman, D.J., Wilkie, W.K.: Temperature-dependent thermoelastic properties for macro fiber composite actuators. J. Therm. Stresses **27**(10), 903–915 (2004)
43. Williams, R.B., Grimsley, B.W., Inman, D.J., Wilkie, W.K.: Manufacturing and mechanics-based characterization of macro fiber composite actuators. In: ASME 2002 International Mechanical Engineering Congress and Exposition, pp. 79–89. American Society of Mechanical Engineers
44. Williams, R.B., Inman, D.J., Schultz, M.R., Hyer, M.W., Wilkie, W.K.: Nonlinear tensile and shear behavior of macro fiber composite actuators. J. Compos. Mater. **38**(10), 855–869 (2004)
45. Deraemaeker, A., Nasser, H., Benjeddou, A., Preumont, A.: Mixing rules for the piezoelectric properties of macro fiber composites. J. Intell. Mater. Syst. Struct. **20**(12), 1475–1482 (2009)
46. Shahab, S., Erturk, A.: Coupling of experimentally validated electroelastic dynamics and mixing rules formulation for macro-fiber composite piezoelectric structures. J. Intell. Mater. Syst. Struct. **28**(12), 1575–1588 (2017)
47. Shahab, S., Erturk, A.: Electrohydroelastic Euler–Bernoulli–Morison model for underwater resonant actuation of macro-fiber composite piezoelectric cantilevers. Smart Mater. Struct. **25**(10), 105007 (2016)
48. Goldschmidtboeing, F., Eichhorn, C., Wischke, M., Kroener, M., Woias, P.: The influence of ferroelastic hysteresis on mechanically excited PZT cantilever beams. In: Proceedings of the 11th International Workshop on Micro and Nanotechnology for Power Generation and Energy Conversion Applications, pp. 114–117
49. Agarwal, B .D., Broutman, L .J., Chandrashekhara, K.: Analysis and Performance of Fiber Composites. Wiley, Hoboken (2006)
50. Crespo da Silva, M .R .M., Glynn, C .C.: Nonlinear flexural-flexural-torsional dynamics of inextensional beams. i. equations of motion. J. Struct. Mech. **6**(4), 437–448 (1978)
51. Malatkar, P.: Nonlinear vibrations of cantilever beams and plates. Thesis (2003)
52. Tan, D., Erturk, A.: In vacuo elastodynamics of a flexible cantilever for wideband energy harvesting. In: SPIE Smart Structures and Materials+ Nondestructive Evaluation and Health Monitoring. International Society for Optics and Photonics, Bellingham
53. Nayfeh, A.H., Mook, D.T.: Nonlinear Oscillations. Wiley, Hoboken (2008)